JOURNAL OF GEOPHYSICAL RESEARCH, VOL. 95, NO. A3, PAGES 2355–2366, MARCH 1, 1990

Three-Dimensional Modeling of Subionospheric VLF Propagation in the Presence of Localized *D* Region Perturbations Associated With Lightning

W. L. POULSEN, T. F. BELL, AND U. S. INAN

STAR Laboratory, Stanford University, Stanford, California

A theoretical model of single-mode, subionospheric VLF wave propagation in the presence of localized perturbations of the nighttime *D* region has been developed. Such perturbations could be produced, for example, by lightning-induced electron precipitation associated with a characteristic type of phase or amplitude perturbation in VLF signals known as "Trimpi" events. Our model assumes that the ionospheric perturbation is slowly varying in the horizontal plane and that mode-coupling is therefore negligible, and accounts for (1) effects of perturbations with finite extent in the dimension transverse to the great circle (GC) path between transmitter and receiver, and (2) effects of perturbations which lie off the GC path as well as on it. The formulation used for the numerical calculations depends significantly on the mode refractive index of the ambient Earth-ionosphere waveguide and the mode refractive index in the region of the perturbation. In the calculations, values for the mode refractive index are determined from the electron-density-versus-altitude profiles of both the ambient and perturbed ionospheres. Values for changes in the amplitude and phase of a received signal were obtained from the model and compared with amplitude and phase measurements of a VLF signal received at Palmer Station, Antarctica, from the NPM transmitter (23.4 kHz) in Hawaii during energetic electron precipitation events. The large distance and all-sea path between the transmitter and receiver make it possible to represent the signal using single waveguide mode theory. The results of varying the location of a perturbation along the GC path as well as off the path in the transverse dimension, varying the horizontal scale of the perturbation, and varying the vertical density profile of the perturbation were all examined. The model shows that positive phase and/or negative amplitude shifts in the received signal are produced by perturbations centered on the GC path, whereas both positive and negative amplitude (or phase) shifts in a single-mode signal can be produced by perturbations lying in regions off the GC path. Results of the model indicate that the magnitude of the signal scattered by the perturbation towards the receiver continuously decreases with distance away from the GC path, becoming insignificant beyond $\sim 20\ \lambda$. On or near the GC path, it was found that the magnitude of the scattered signal was proportional to the scale of the perturbation parallel to the GC path. Using realistic values for the ground and ionospheric profile parameters, values of the shift in the amplitude and phase of the signal similar to those measured on the NPM signal received at Palmer Station, Antarctica, were obtained using this model. For example, a cylindrically symmetric perturbation of 5 λ in horizontal extent due to a 0.2 second burst of precipitating electrons of $\sim 2 \times 10^{-3}$ ergs cm^{-2} s^{-1} flux density can produce amplitude changes of ~ -0.3 dB and phase changes of $\sim 2^{\circ}$. Results from the model suggest that the ratio of the shifts in signal phase and amplitude can be used to determine the distance of the perturbation from the GC path.

1. INTRODUCTION

Subionospheric VLF probing has recently emerged as a powerful remote sensing tool for studying transient ionospheric perturbations associated with lightning-generated whistlers [*Inan and Carpenter*, 1986, 1987] or with lightning discharges [*Inan et al.*, 1988*a*, *b*]. The phenomenon is referred to as the "Trimpi" effect, in which phase and/or amplitude perturbations in subionospheric VLF radio signals occur in response to secondary ionization generated in the lower ionosphere by lightning-induced electron precipitation (LEP) bursts [*Helliwell et al.*, 1973; *Lohrey and Kaiser*, 1979] (see Figure 1*a*).

Quantitative interpretation and understanding of lightning-associated VLF perturbation events must be based on a model of subionospheric VLF propagation in the presence of localized density enhancements in the nighttime *D* region. Initial theoretical models have treated the Earth-ionosphere waveguide, in which the VLF signal propagates, as infinite in the horizontal dimension transverse to the direction of propagation [*Tolstoy*, 1983; *Inan et al.*, 1985; *Tolstoy et al.*, 1986; *Inan and Carpenter*, 1987]. In this picture, the perturbation is assumed to lie on the great circle (GC) path of propagation, and is assumed to be infinite in the transverse dimension. The problem is thus reduced to one having two dimensions: the height of the waveguide and the distance along the path of propagation as depicted in Figure 1*a*. Analysis of some of the experimental data has indicated the need for a more general treatment. *Carpenter and LaBelle* [1982] found that perturbations associated with ducted whistlers can at times be located at significant distances (up to ~200 km) transverse to the GC path between transmitter and receiver, and *Inan and Carpenter* [1987] recognized the need for more realistic models which include the effects of off-GC-path locations of ionospheric perturbations. Recently, *Dowden and Adams* [1988, 1989] have put forward a heuristic three-dimensional model based on 'echoes' from lightning-induced electron precipitation (LEP) ionization 'patches' or ridges located off the GC path.

Paper number 89JA02920.
0148-0227/90/89JA-02920$05.00

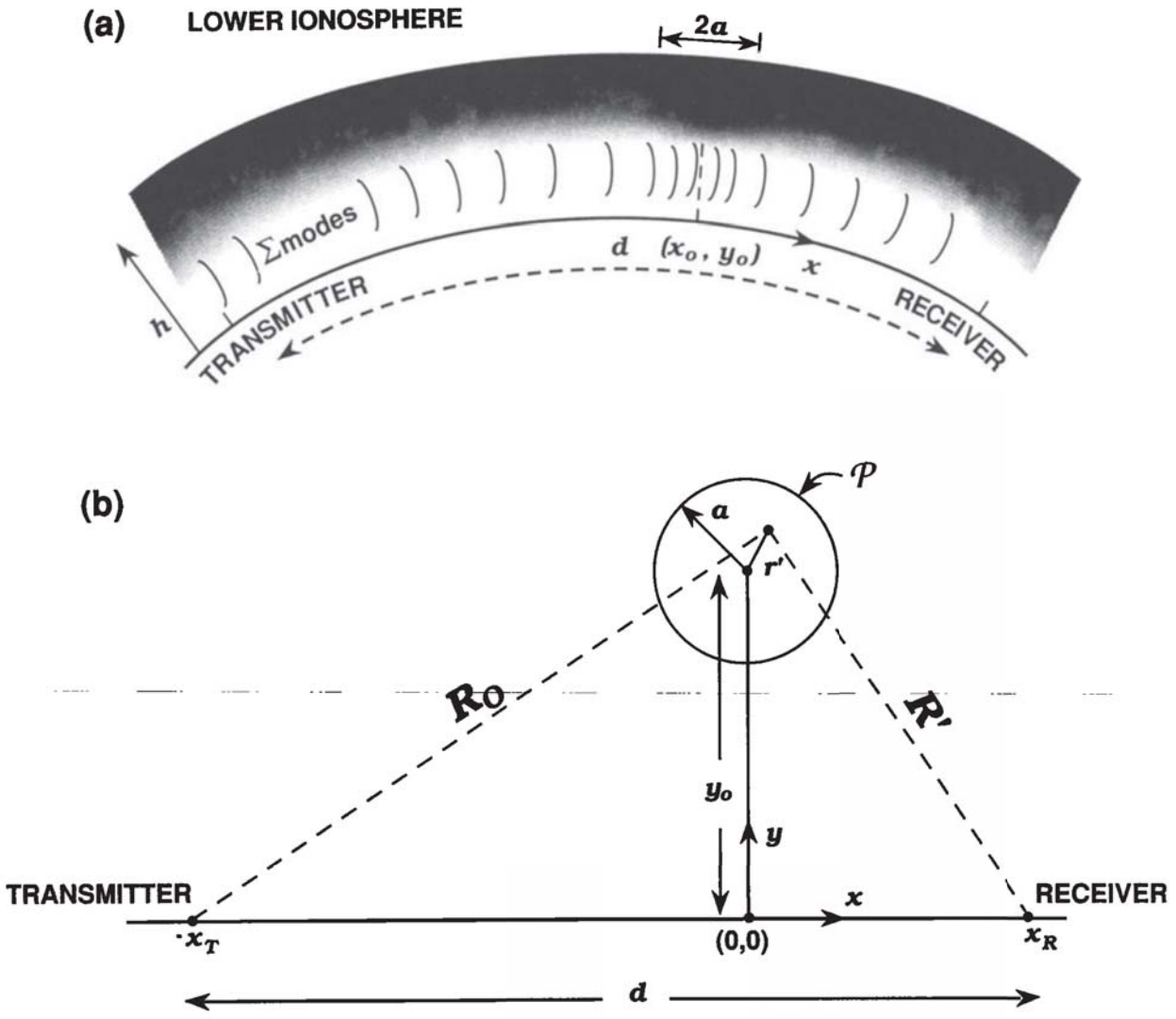

Fig. 1. (*a*) Side view representation of the Earth-ionosphere waveguide between a transmitter and receiver separated by a distance d along the surface of the Earth. The change in the electron density with altitude h of the lower ionosphere is represented by the change in shading density. Also represented is a density enhancement region or perturbation of the ambient ionosphere such as those generated by lightning-induced electron precipitation bursts. The center of this perturbation is located at the point (x_o, y_o). Such a perturbation, appearing transiently, scatters some of the signal impinging on it and causes a temporary perturbation in the total signal measured at the receiver. (*b*) A plan view, seen from above, of the situation depicted in Figure 1*a* showing the three-dimensional configuration of the problem and identifying the geometry and variables used in equations (6)–(12). Note that the origin has been shifted to the point $x = x_o$.

In this paper we present a three-dimensional model based on an analysis of VLF propagation in the Earth-ionosphere waveguide in the presence of ionospheric perturbations of various types [*Wait*, 1961, 1964*a*, 1964*b*]. Although in the general case wave propagation would be analyzed in terms of a sum of modes travelling in the spherical waveguide formed by the Earth's surface and the lower ionosphere, the preliminary model presented here is restricted to single mode propagation. Using first-order scattering theory [*Wait*, 1964*a*] to determine the expected field under the influence of ionospheric perturbations, numerical analyses are made of cases where single mode analysis may be applicable. One such case is the problem of 10–25 kHz wave propagation over a long, all-sea-based path from the source to the receiver. If the ionospheric perturbation satisfies the WKB approximation [*Budden*, 1985], this problem reduces to the analysis of a single 'dominant' mode at the receiver. Theoretical results are compared with measurements of Trimpi events observed at Palmer Station, Antarctica on the 23.4 kHz signal from the NPM transmitter in Hawaii arriving on a 12,000-km long all-sea-based path [*Inan and Carpenter*, 1987].

2. THEORY

In this section, we present a brief discussion of the problem formulation and the theoretical basis for the expressions used in the numerical calculations.

Secondary Modal Electric Field 'Scattered' by an Ionospheric Perturbation

Wait [1962] showed that under undisturbed ionospheric conditions, with the Earth and the ionosphere taken to be spherically concentric, and with homogeneous conditions along the entire path, the vertical electric field E at a great circle (GC) path distance d from a transmitter can be written as a sum of modes in the form

$$E = \left[\frac{1}{\sin(d/R_e)}\right]^{\frac{1}{2}} \sum_n A_n e^{-ik_0 S_n d} \tag{1}$$

where R_e is radius of the Earth, $k_0 = 2\pi/\lambda_0$ where λ_0 is the free space wavelength of the signal, and S_n is equivalent to the complex index of refraction for mode n, and thus determines the attenuation and phase velocity of that mode. In the general case, S_n is a function of the waveguide properties at each point along the path. A_n is a complex-valued function which includes the excitation and the height-gain factors at the transmitter and receiver and is dependent only on the conditions at the transmitter and receiver locations.

This expression can be generalized to include slow variations in the local properties of the Earth-ionosphere waveguide in both the GC path direction (x direction) and the transverse direction (y direction), in which case S_n becomes a function of x and y. (See Figure 1*b*.) The expression for the total field a distance d from the transmitter then has the form [*Wait*, 1964*a*]

$$E \simeq \left[\frac{d/R_e}{\sin(d/R_e)}\right]^{\frac{1}{2}} \sum_n [A_n(0)A_n(d)]^{\frac{1}{2}}\, e_n \tag{2}$$

where

$$e_n \simeq \left\{\frac{1}{\sqrt{x/R_e}} \exp[-ik_0 \int_C S_n(x', y')ds]\right\}_{x=d} \tag{3}$$

the origin ($x = 0, y = 0$) is located at the transmitter, and the integration contour C is along the path of minimum total phase between the transmitter and observation point at d.

The above expression assumes that the properties of the Earth-ionosphere waveguide are slowly varying in the horizontal (x and y) directions so that the conversion of modes from one order to another, i.e., mode coupling, can be safely ignored. This assumption is justified if the waveguide properties do not change appreciably in a horizontal distance of one wavelength [*Wait*, 1964*a*] and if each mode n has relatively low attenuation, i.e.,

$$\text{Im}\,[S_n(x, y)] \ll 1 \tag{4}$$

The modal field e_n satisfies a two-dimensional Helmholtz equation of the form

$$\left[\frac{\partial^2}{\partial x^2} + \frac{\partial^2}{\partial y^2} + (k_0 S_n)^2\right] e_n = 0 \tag{5}$$

for each mode of order n. Using a perturbation method, and assuming that mode coupling effects do not occur and that Earth curvature effects are negligible, the solution of equation (5) for each modal field e_n is found to be [*Wait*, 1964*a*]

$$\begin{aligned} e_n(x, y) &= e_n^0(x, y) + e_n^s(x, y) \\ &= e_n^0(x, y) - \frac{ik_0^2}{4} \iint_{\mathcal{P}} \left[S_n^2(x', y') - (S_n^0)^2\right] \\ &\quad \times e_n(x', y') H_0^{(2)}(k_0 S_n^0 R') dx' dy' \end{aligned} \tag{6}$$

where e_n is the total modal field for the mode of order n (i.e., the total field seen at (x, y) in the presence of some perturbation of the waveguide); e_n^0 is the unperturbed modal field, also called the 'direct' field, (i.e., the field seen in the absence of any perturbation); e_n^s is the secondary or 'scattered' field, (i.e., the field seen at (x, y) produced by the perturbation); S_n^0 is the ambient value of S_n in the absence of any perturbation, and in this analysis is a constant independent of x and y; $\mathcal{P}$ is the region of integration, or 'patch', which extends over that portion of the x-y plane that encompasses the perturbation (i.e., where $S_n \neq S_n^0$); $H_0^{(2)}$ is a Hankel function of the second kind of order zero; and

$$R' = \sqrt{(x - x')^2 + (y - y')^2} \tag{7}$$

In order to simplify the evaluation of (6), we shift the origin from the transmitter location to the point $x = x_o$ along the GC path between transmitter and receiver. A plan view of the geometry is shown in Figure 1*b*. The origin is located such that the transmitter coordinates are $(-x_T, 0)$ and the location where the field e_n is observed, i.e., the receiver coordinates, are $(x_R, 0)$. Thus, $R' = \sqrt{(x_R - x')^2 + (y')^2}$ and $d = x_T + x_R$.

An approximate solution of (6) can be found by substituting the unperturbed field e_n^0 for the total perturbed field e_n inside the integral (known as the Born approximation). This substitution is justified if S_n inside the perturbation region $\mathcal{P}$ is only slightly different from the 'background', or unperturbed, value S_n^0 (i.e., $|S_n - S_n^0| \ll 1$), a condition that holds for the various ionospheric electron density profiles considered in this paper. From (3) it can be shown that the unperturbed field e_n^0 at a distance R_o from the transmitter and at a location (x', y') has the form

$$e_n^0(x', y') \simeq \frac{K}{\sqrt{R_o}} e^{-ik_0 S_n^0 R_o} \tag{8}$$

where for the geometry shown in Figure 1*b*, K is a constant factor and

$$R_o = \sqrt{(x_T + x')^2 + (y')^2} \tag{9}$$

For locations (x, y) greater than approximately one wavelength from the transmitter or receiver, the asymptotic form of the Hankel function as given below can be used in (6).

$$H_0^{(2)}(k_0 S_n^0 R') \simeq \left[\frac{2i}{\pi k_0 S_n^0 R'}\right]^{\frac{1}{2}} e^{-ik_0 S_n^0 R'} \tag{10}$$

With the above-mentioned assumptions and substitutions, the expression for the scattered modal field seen at the receiver, $e_n^s(x_R, 0)$, normalized by the unperturbed modal field that would have been seen at the receiver in the absence of a perturbation, $e_n^0(x_R, 0)$, is

$$\begin{aligned} \left.\frac{e_n^s}{e_n^0}\right|_{(x_R,0)} &\simeq \frac{-ik_0^2}{4}\sqrt{\frac{i2d}{\pi k_0 S_n^0}} \iint_{\mathcal{P}} \frac{\left[S_n^2(x', y') - (S_n^0)^2\right]}{\sqrt{R_o R'}} \\ &\quad \times e^{-ik_0 S_n^0 (R_o + R' - d)} dx' dy' \end{aligned} \tag{11}$$

where d is the GC path distance between the transmitter and receiver. For the purposes of this study the region $\mathcal{P}$ is assumed to be circular with radius a, and because of circular symmetry, $S(x', y')$ becomes $S(r')$ [*Wait*, 1964*b*]. Thus, the assumed geometry is as shown in Figure 1*b*, and after making the substitutions $x' = r' \sin\theta'$ and $y' = y_o + r' \cos\theta'$, equation (11) can be rewritten as

$$\left.\frac{e_n^s}{e_n^o}\right|_{(x_R,0)} \simeq \frac{-ik_o^2}{4}\sqrt{\frac{i2d}{\pi k_o S_n^o}}\int_0^{2\pi}\int_0^a \frac{\left[S_n^2(r') - (S_n^o)^2\right]}{\sqrt{R_o R'}} \times e^{-ik_o S_n^o(R_o+R'-d)} r' dr' d\theta' \quad (12)$$

For a circular perturbation of the ionosphere of radius a, located at (x_o, y_o), and for a given frequency, a (complex) value for the field scattered by the perturbation relative to the 'direct' signal can be determined numerically from (12) if the background index of refraction S_n^o and the perturbed index of refraction $S_n(r')$ are known.

The relationship between e_n^s and e_n^o can be illustrated by using a phasor diagram as pictured in Figure 2 [*Dowden and Adams*, 1988]. The difference between the length of e_n and the length of e_n^o represents the change in amplitude (ΔA) caused by e_n^s. The difference between the phase angles $\angle e_n$ and $\angle e_n^o$ represents the change in phase ($\Delta\phi$) caused by e_n^s. These two quantities, ΔA and $\Delta\phi$, are the relevant quantities measured in Trimpi events; and theoretical values for ΔA and $\Delta\phi$ as would be observed at the receiver can be readily computed from the (complex) value of e_n^s/e_n^o determined from (12).

Determination of the Mode Refractive Indices S_n and S_n^o

The complex quantities S_n and S_n^o can be computed using the mode theory of VLF propagation in the Earth-ionosphere waveguide [*Wait*, 1962]. In this theory, the energy within the waveguide is considered to be partitioned among a series of modes. Each mode is associated with one of a discrete set of angles of incidence θ_n of the waves on the ionosphere, for which constructive interference occurs and energy propagates away from the source. This set of complex eigenangles gives the solutions to the modal equation [*Morfitt and Shellman*, 1976]

$$\left|\mathbf{R}_h^i(\theta_n)\mathbf{R}_h^g(\theta_n) - \mathbf{I}\right| = 0 \quad (13)$$

where $\mathbf{I}$ is the identity matrix, $\mathbf{R}_h^i(\theta_n)$ is the complex-valued reflection coefficent matrix looking up into the ionosphere from height h, and $\mathbf{R}_h^g(\theta_n)$ is the complex-valued reflection coefficient matrix looking down towards the ground from height h. The elements of the two reflection coefficient matrices are determined by integration of differential equations which describe the coefficients as a function of the properties of the Earth and the ionosphere 'boundaries' at a given location [*Budden*, 1955, 1961; *Sheddy*, 1968].

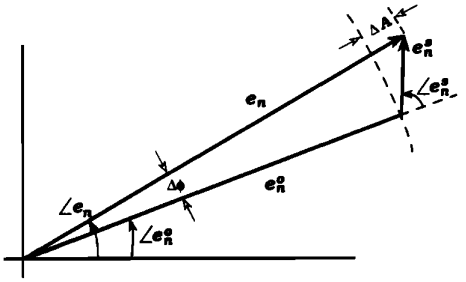

Fig. 2. Phasor diagram illustrating the relationship between the total signal modal field e_n, the direct, or unperturbed, signal modal field e_n^o, and the scattered signal modal field e_n^s. The two quantities important in the discussion of the results, ΔA (change in amplitude) and $\Delta\phi$ (change in phase), are indicated. The phase angles $\angle e_n$ and $\angle e_n^o$ are measured with respect to the same (arbitrary) reference.

The complex quantities S_n and S_n^o are simply the (complex-valued) sines of the eigenangles θ_n that satisfy equation (13) (i.e., $S_n = \sin\theta_n$) for the appropriate waveguide conditions and properties at the perturbed, and background, ionosphere, respectively [*Wait*, 1962].

Since the solutions to the modal equation (13) cannot be determined in closed form, we use the computer program "MODEFNDR" [*Morfitt and Shellman*, 1976; *Shellman*, 1986; *Ferguson and Snyder*, 1987] developed by the Naval Ocean Systems Center (NOSC) to obtain values for S_n and S_n^o numerically. The input to this program consists of arbitrarily assigned electron and ion density distributions with height, as well as collision frequency profiles, the anisotropy of the ionosphere, ground conductivity and permittivity, and accounts for the curvature of the Earth. Using these quantities, MODEFNDR solves the modal equation (13) for the θ_n from which S_n (or S_n^o) are determined.

3. RESULTS

In this section we present some numerical results obtained for three different ionospheric perturbation profiles as shown in Figure 3. Profiles I, II, and III represent the electron density at the location of maximum perturbation (x_o, y_o) as a function of altitude h resulting from electron precipitation bursts induced by lightning-generated whistlers propagating at $L = 2$, 2.5, and 3, respectively [*Inan et al.*, 1988*a*]. The ambient nighttime D region electron density profile that is used is also shown for reference. The total precipitating electron energy flux density for each profile was adjusted

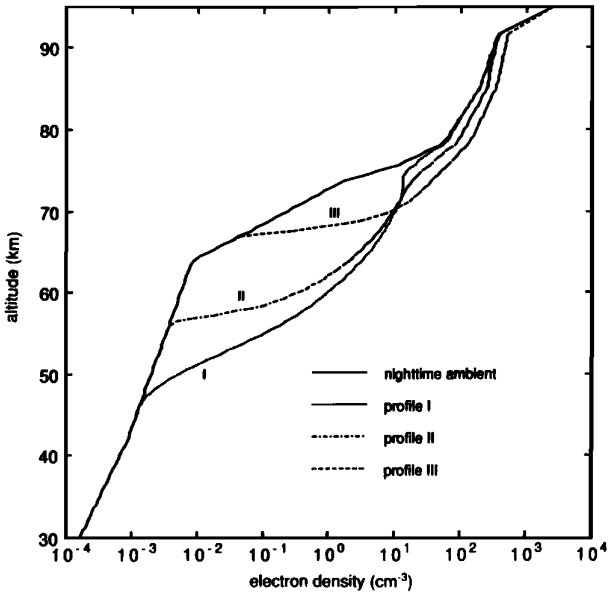

Fig. 3. Plot of the ambient electron density distribution with altitude and three different ionospheric perturbation profiles used in the calculations. Profiles I, II, and III represent the electron density distribution with altitude at the location of maximum perturbation (x_o, y_o) resulting from electron precipitation bursts induced by lightning-generated whistlers propagating at $L = 2$, 2.5, and 3, respectively. The total precipitating electron energy flux density for each profile has been adjusted such that the value of $|S_n - S_n^o|$ produced by each perturbed profile is the same. A typical value of 200 ms for the duration of the lightning discharge and the subsequent LEP burst has been assumed in the profile generation.

so that the magnitude of the difference between the mode refractive index S_n corresponding to each profile and the ambient mode refractive index S_n^0 (corresponding to the ambient density profile) was the same; i.e., $|S_n - S_n^0|$ has been normalized to the same value for all three perturbed profiles shown in Figure 3. The resulting energy flux densities required to produce these profiles range from $\sim 2 \times 10^{-3}$ ergs cm^{-2} s^{-1} for $L = 2$ to $\sim 4 \times 10^{-2}$ ergs cm^{-2} s^{-1} for $L = 3$. The rationale behind this normalization will be discussed below.

The difference between the perturbed electron density $N_e(h)$ and the ambient nighttime density $N_e^0(h)$ is designated by $\Delta N_e(h)$. The variation of $\Delta N_e(h)$ with distance in the horizontal direction r' (see Figure 1*b*) is represented by a cylindrically symmetric Gaussian distribution such that

$$\Delta N_e(r', h) = \Delta N_e(x_o, y_o, h) e^{-(\frac{r'}{a})^2} \tag{14}$$

where $r' = [(x' - x_o)^2 + (y' - y_o)^2]^{\frac{1}{2}}$ and the parameter a is the effective 'patch' radius. In general, the refractive index $S_n(r')$ depends on density in a complex manner. However, analysis indicates that, for the parameter ranges considered, an approximate expression for $S_n(r')$ can be written as

$$S_n(r') = [S_n(0) - S_n^0] e^{-(r'/a)^2} + S_n^0 \tag{15}$$

Simplified analytic solutions of equation (11) are derived in the Appendix assuming that (14) and (15) apply.

The results presented below were obtained by numerical evaluation of equation (12) using realistic values for the different parameters d, a, y_o, x_T or x_R, S_n^0, and $S_n(r')$. All distances were normalized to units of wavelength (λ) and the following assumptions were made to facilitate comparison with published data:

1. A long ($d = 800$ λ), all-sea-based signal path from source to receiver (thereby making 'ground' conductivity and permittivity constant).

2. A single ambient density profile $N_e^0(h)$ for the lower ionosphere. Typical values of ambient density were obtained from the International Reference Ionosphere [*Rawer et al.*, 1978] for altitudes down to 95 km, below which, the ambient profile was assumed to have the form shown in Figure 3.

3. A single dominant mode arriving at the receiver. (For an 800-λ-long all-sea path at 20 kHz ($\lambda = 15$ km), our calculations show the $n = 2$ field component to be 8 dB higher than the $n = 1$ component.)

4. A single perturbation patch having the general shape described in (14).

5. Negligible mode coupling in the perturbed region.

With these assumptions equation (12) was evaluated for (1) a series of patch radii a ranging from 0.15 λ to 10 λ (equivalent to a range of 2.3 km to 150 km at 20 kHz), (2) a series of patch location distances in the x direction (x_T) ranging from points 10 λ from the transmitter to the path midpoint, i.e., 400 λ in this case (equivalent to a range of 150 km to 6000 km at 20 kHz), and (3) a series of patch locations in the y direction (y_o) ranging from 0 to 20 λ (equivalent to a range of 0 to 300 km at 20 kHz).

Since equation (12) is symmetric both in the x direction about the midpoint of the GC path and in the y direction to either side of the GC path, a single 'quadrant' of the x-y plane between the transmitter and the receiver provides all non-redundant information about the received signal.

Numerical results for a few of the cases discussed above are presented in Figures 4–6. Figure 4 is a contour plot of the calculated change in amplitude (ΔA) and change in phase ($\Delta\phi$) seen at the receiver that would be produced by a perturbation whose center location (x_o, y_o) is scanned in both the x and y directions over the range of values mentioned above. The result shown is for the perturbation density profile I (Figure 3) and an effective patch radius a of 5 λ. Figure 5 is a 'slice' along the y direction of Figure 4 for a fixed value of x ($x/d = 0.25$ in this example) but parametric in a which shows the dependence of ΔA and $\Delta\phi$ on distance away from the GC path (i.e., in the y direction). Figure 6 shows the y dependence of the magnitude and phase of the secondary field e_n^s, again at $x/d = 0.25$ and parametric in a. Several interesting aspects of the results are noted as follows:

1. Perturbations centered on the GC path produce an advance in the phase and/or a reduction in the amplitude of the received signal. For perturbations located off the GC path, any combination of positive or negative, amplitude or phase changes is possible depending on the patch location with respect to the transmitter or receiver, and to the GC path. (See Figure 5.)

2. The magnitude of the scattered modal field e_n^s continuously decreases with distance off the GC path (i.e., the y direction) as shown in Figure 6, becoming insignificant beyond ~ 20 λ. In terms of the phasor diagram shown in Figure 2, the length of the e_n^s vector continuously shrinks as the patch moves away from the GC path and thus the largest value of ΔA or $\Delta\phi$ possible becomes smaller.

3. At a given patch location (x_o, y_o), the amplitude of e_n^s is found to depend significantly on the following items: (1) The magnitude of the difference, ΔS, between the mode refractive index at the peak of the perturbation $S_n(0)$ and the 'background' mode refractive index S_n^0 (in other words, $|\Delta S| = |S_n(0) - S_n^0|$). The value of ΔS depends on the perturbation density profile used and on which mode is dominant at the perturbation. For the range of parameters considered, it was found that $|e_n^s|$ was proportional to $|\Delta S|$ It was also found that a given perturbation density profile generally produced different e_n^s for each waveguide mode. Thus, the effect produced by a given perturbation will depend upon which mode is dominant at the patch location. (2) The horizontal extent of the perturbation patch. Near the GC path, as the radius a of the patch is increased, the magnitude of e_n^s is found to increase also (see Figure 6). Thus, the larger the patch size, the larger the total VLF perturbation that is produced. However, at certain points either of the perturbation components ΔA, or $\Delta\phi$, may decrease as a increases (see Figure 5).

4. A perturbation density enhancement that penetrates to lower altitudes is found to cause larger changes in amplitude, yet smaller changes in phase, than a density enhancement that lies at a higher altitude having the same magnitude of ΔS as the deeply penetrating perturbation. Because of the dependence of $|e_n^s|$ on $|\Delta S|$, the density enhancement profiles shown in Figure 3 were normalized to the same $|\Delta S|$ in order to compare the differences in ΔA and $\Delta\phi$ caused by the different profiles. In the context of lightning-induced electron precipitation, lightning-generated whistlers of constant frequency range propagating at lower L-shells induce precipitation bursts that penetrate more deeply than do bursts induced by whistlers of the same frequency range propagating at higher L-shells (see Figure 3). This is illustrated in Figures 7*a* and 7*b*, which show curves of ΔA and $\Delta\phi$ calculated for a patch with effective radius of 5 λ, where

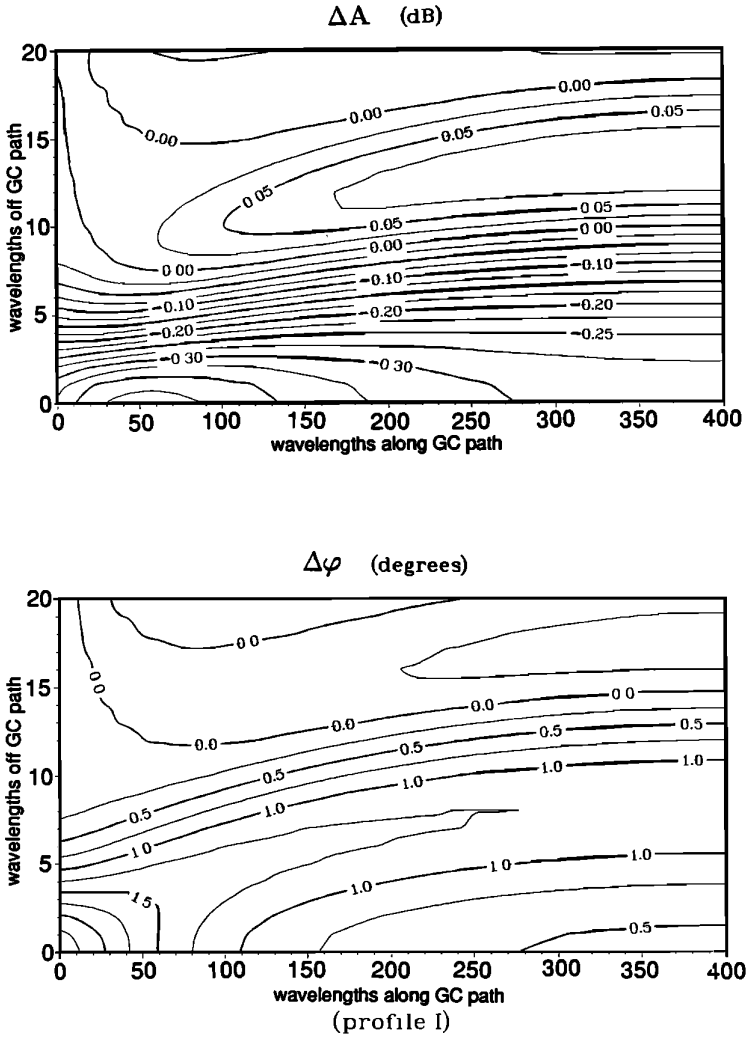

Fig. 4. Contour plots of the calculated ΔA and $\Delta\phi$ seen at the receiver that would be produced by a circularly symmetric perturbation with a horizontal Gaussian distribution whose center is moved in both the x (along the GC path) and y (off the GC path) directions over a range of values along the GC path of 10 λ from the transmitter (or receiver) to the path midpoint (400 λ), and over a range of values off the GC path of 0 λ to 20 λ away. The results shown were calculated using profile I of Figure 3 and an effective patch radius a of 5 λ. The y dimension has been exaggerated for clarity.

each of the three curves in each plot are calculated for a perturbation patch having one of the three density profiles shown in Figure 3. Figure 7*a* shows the value of ΔA or $\Delta\phi$ along the GC path itself, and Figure 7*b* shows the value of ΔA or $\Delta\phi$ away (in the y direction) from a GC path point one-fourth of the total GC path distance from the transmitter (or receiver). Comparing the curves in each plot, it can be seen that profile I of Figure 3, representing a perturbation at $L = 2$, produces greater maximum values of $|\Delta A|$ and smaller maximum values of $|\Delta\phi|$ than does profile III of Figure 3 representing a perturbation at $L = 3$ (with the same value of $|\Delta S|$ as profile I).

5. The values of ΔA and $\Delta\phi$ can be used to roughly determine the distance y_o from the GC path to the perturbation. For example, $\Delta A \sim 0$ when $y_o \sim 8\lambda$ for an effective patch radius of 5 λ. (See Figure 4.)

4. Discussion and Comparison

Inan and Carpenter [1987] presented initial results of phase and amplitude measurements of the NPM signal received at Palmer Station, Antarctica. The NPM transmitter frequency is 23.4 kHz ($\lambda = 12.8$ km) along an all-sea GC path of ~12,335 km (or 964 λ), and the unperturbed signal at the receiver for these parameters consists basically of a single, dominant mode. *Inan and Carpenter* [1987] found that the distribution of phase perturbations typically peaked around $\Delta\phi \simeq 2.5°$, and that the overwhelming percentage (> 95%) of the events observed were positive phase, negative amplitude perturbations. More recent measurements [*Wolf*, 1990] showed similar results and also found that the distribution of amplitude perturbations seen at Palmer typically peaked around $\Delta A \simeq -0.3$ dB. Our numerical results indi-

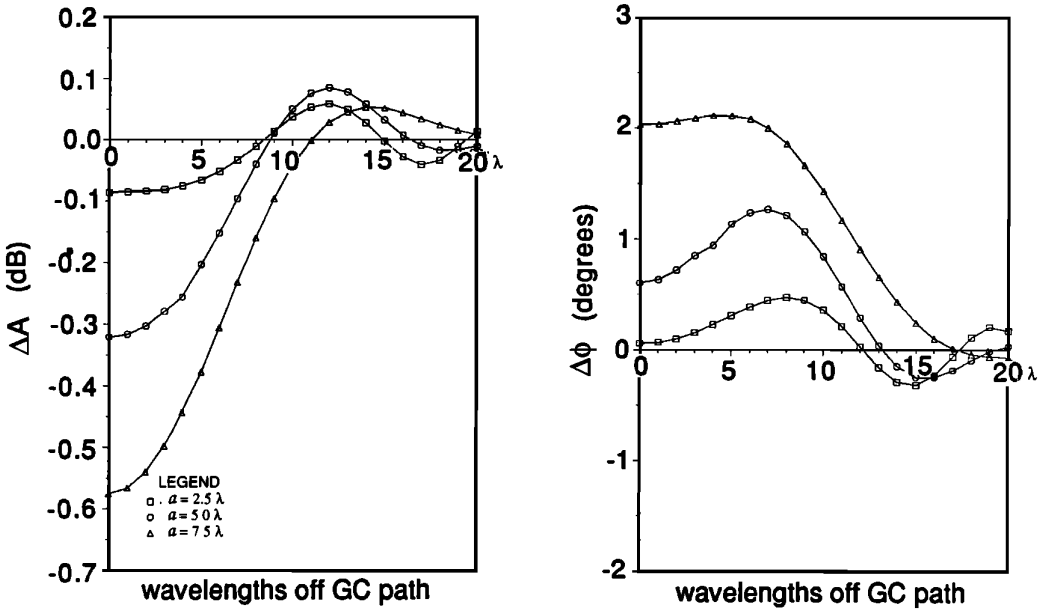

Fig. 5. Two-dimensional 'cut' along the y direction of Figure 4 taken at a fixed value along the x axis ($x_T/d = 0.25$ in this case) showing the dependence of ΔA and $\Delta\phi$ on distance (in wavelengths) away from the GC path for three different values of effective radius a.

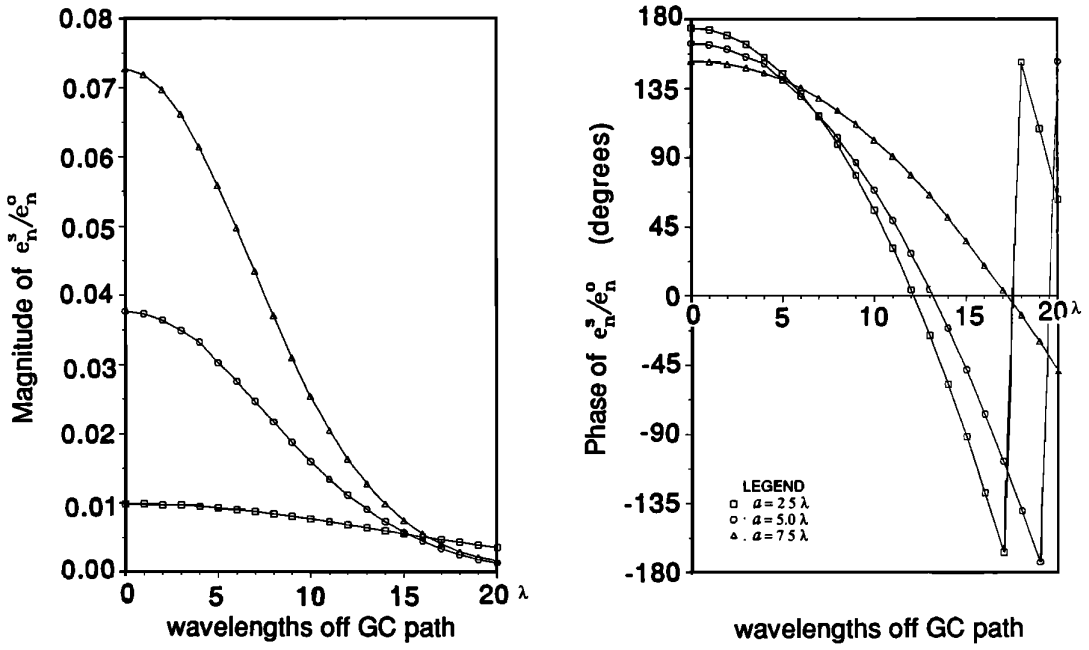

Fig. 6. Plot showing the dependence of the magnitude and phase of the scattered signal e_n^s on distance (in wavelengths) away from the GC path for the same values of a and x_T/d as in Figure 5 and again using profile I of Figure 3. The values of $|e_n^s|$ and $\angle e_n^s$ are relative to those of the direct signal e_n^o.

cate that perturbation patches centered on or near the GC path always produce positive $\Delta\phi$ and negative ΔA values, and that the strongest magnitude scattered signal strength is produced by patches closest to the GC path. Thus, it appears that most Trimpi events seen on the NPM–Palmer signal may be due to perturbations located close to or on the GC path.

It is of interest to consider the distribution of $|\Delta A|$ and $|\Delta\phi|$ over long time periods where the perturbation might appear at a wide range of locations. Figures 8*a* and 8*b* show plots of $|\Delta A|$ versus $|\Delta\phi|$ for a variety of patch sizes a and a regularly spaced grid of patch locations (x_o, y_o) for two specific perturbed density profiles $N_e(r', h)$, (profiles I and III of Figure 3, respectively). These figures are similar to Fig-

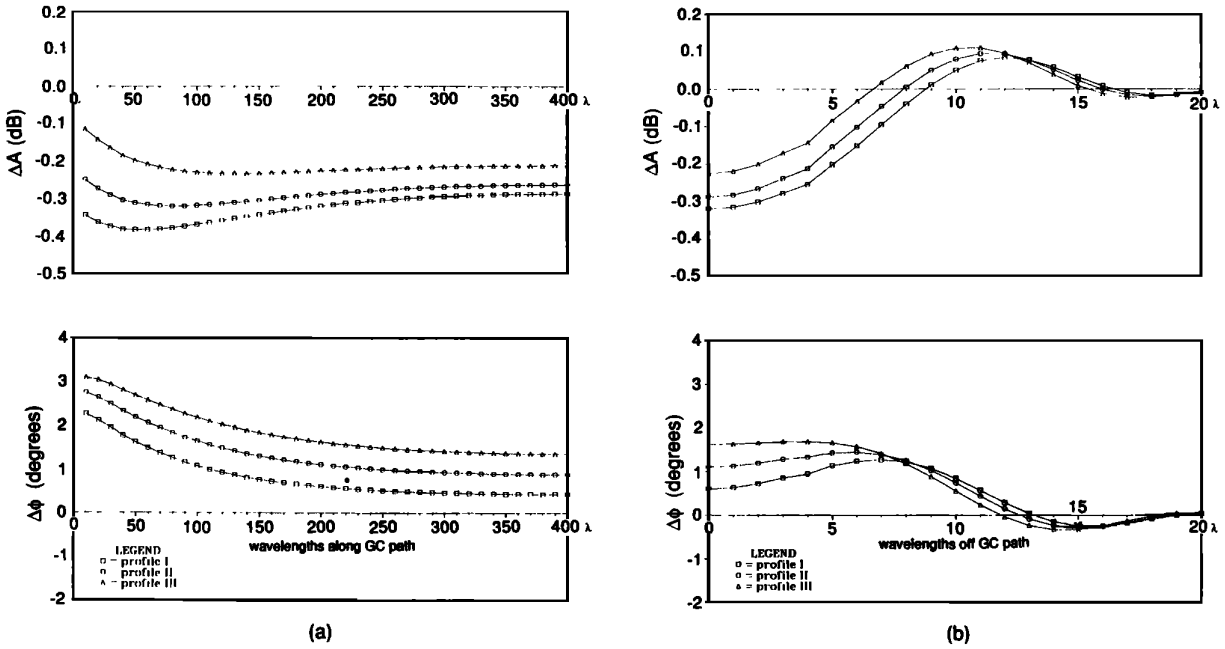

Fig. 7. (*a*) Plots of ΔA and $\Delta\phi$ similar to those shown in Figure 5 except the two-dimensional 'cut' is taken along the x direction of Figure 4, along the GC path (i.e., for a fixed value along the y axis of $y_o = 0$). The effective radius a is fixed at 5 λ and the three different curves of ΔA and $\Delta\phi$ are calculated using the three different perturbed density profiles of Figure 3. (*b*) Plots of ΔA and $\Delta\phi$ versus y similar to those shown in Figure 5 except that the effective radius was fixed at $a = 5$ λ and the three curves shown represent the changes produced by the three density profiles of Figure 3 (the same as in Figure 7*a*). Again, x_T/d was fixed at 0.25 in this example.

ure 11*a* of *Inan and Carpenter* [1987] or Figure 7 of *Dowden and Adams* [1988]; however, the results shown in Figure 8 do not take into account the relative probability of occurrence of different size LEP patches nor the relative probability of occurrence of different locations of the patch with respect to the signal path. Rather, they show a range of ΔA-versus-$\Delta\phi$ values produced by a given perturbed density profile that can be expected on the basis of the present theory. In comparing Figure 8*a* with Figure 11*a* of *Inan and Carpenter* [1987], we note that the theoretical results are computed for a selected range of parameters that represent typical circumstances. In particular for Figure 8*a*, a range of patch radii a from 3.75 λ to 10 λ only was used together with the same density profile (profile I of Figure 3) for all of the values of the points. Profile I represents an energy flux density of $\sim 2 \times 10^{-3}$ ergs cm^{-2} s^{-1} occurring at $L = 2$. Patch radii a larger than 10 λ and/or energy flux densities greater than $\sim 2 \times 10^{-3}$ ergs cm^{-2} s^{-1} would lead to $|\Delta A| > 0.9$ dB and/or $|\Delta\phi| > 6°$. Any discrepancies between our Figure 8*a* and Figure 11*a* of *Inan and Carpenter* [1987], for example the fact that a number of the measured data points of *Inan and Carpenter* [1987] have $|\Delta A| > \sim 0.9$ dB or $|\Delta\phi| > \sim 6°$ can be easily attributed to such variations in the parameter ranges.

While previous work considered the ionospheric perturbations in terms of a reflection height change, our results illustrate the critical dependence on the perturbed ionospheric density profile. One result is that the ratio of amplitude change to phase change, i.e., $|\Delta A/\Delta\phi|$, is larger for perturbed density enhancements lying at lower altitudes, such as what would be produced by LEP bursts at lower L-shells (e.g., see profile I of Figure 3) than for those lying at higher altitudes and corresponding to LEP events at higher L-shells (e.g., see profile III of Figure 3). This result is seen by comparing Figures 8*a* and 8*b*. Since the values plotted in Figure 8*a* correspond to a perturbed density enhancement lying at a lower altitude than that of the values plotted in Figure 8*b* (i.e., profile I versus profile III of Figure 3), the ratio $|\Delta A/\Delta\phi|$ of points in Figure 8*a* is larger than such a ratio of the corresponding points in Figure 8*b* (Figures 8*a* and 8*b* differ only in the perturbed density profile used in their calculation). As a consequence, it can be seen that the 'average' slope of the envelope of the points plotted in Figure 8*a* is higher than that of the envelope of points plotted in Figure 8*b*.

Another interesting feature of our results relating to the use of electron density profiles rather than effective reflection height changes is that the ionospheric perturbations shown in Figure 3 do not actually lead to significant changes in reflection height for the waveguide modes. For example, the maximum change in reflection height in our model is produced by profile III and has the small value $\Delta h \sim 2$ km. Thus, the waveguide perturbations in our model are produced mainly by the ionization which lies below the reflection height, and the actual change in reflection height is a secondary effect in producing the perturbations. In view of this circumstance, we believe that it can be very physically misleading to describe waveguide perturbations in terms of effective reflection height changes.

Dowden and Adams [1988] suggest that the Trimpi events they studied were produced by small LEP patches, and that there was no statistical correlation between the 'echo' (scat-

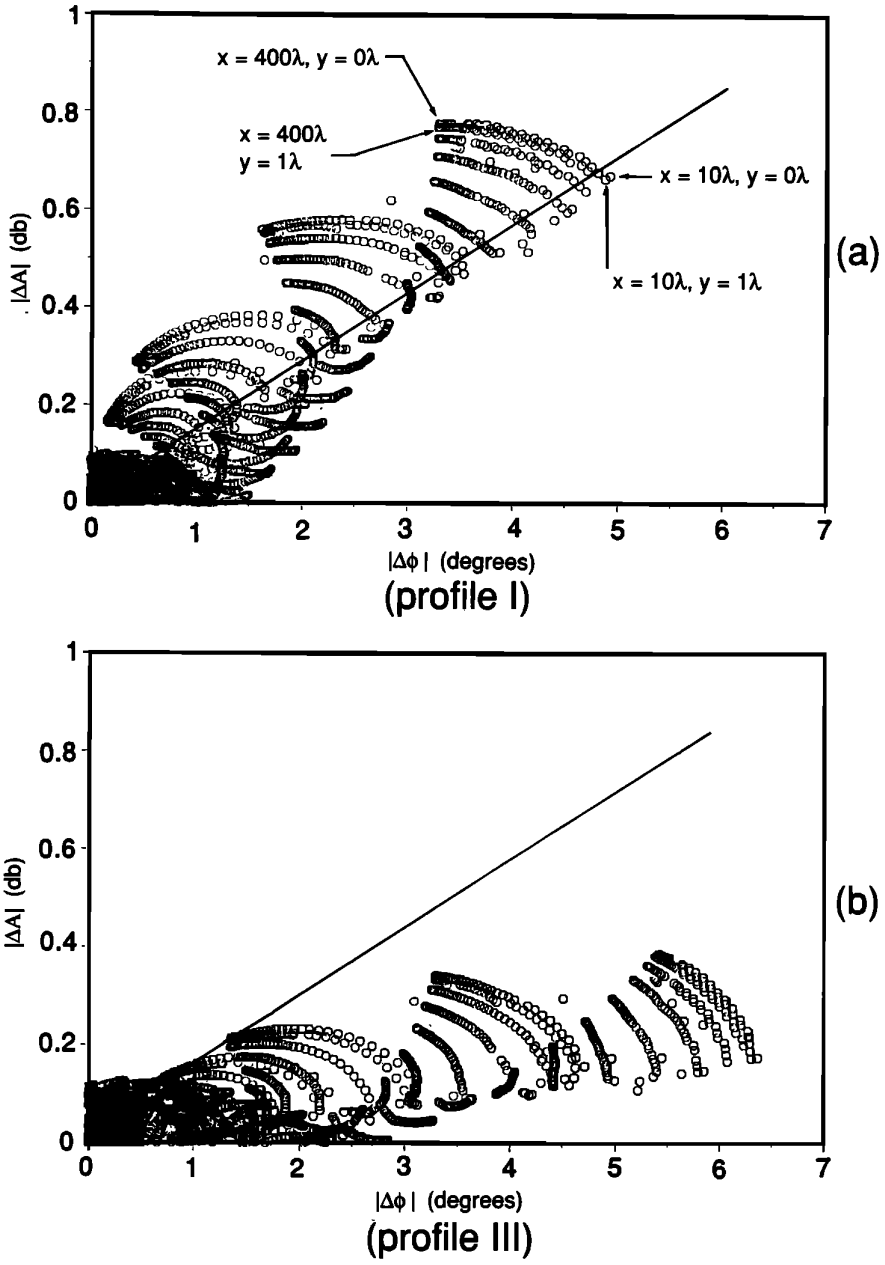

Fig. 8. (*a*) A plot of calculated values of $|\Delta A|$ versus $|\Delta\phi|$ for a range of patch radii a from 3.75 λ to 10 λ, and a regularly spaced grid of patch locations (x_o, y_o) spaced 10 λ apart in the x direction (ranging from 10 λ to 400 λ away from the transmitter or receiver) and 1 λ apart in the y direction (ranging from on the GC path to 20 λ off the GC path) for perturbed density profile I of Figure 3. Arrows indicate calculated values corresponding to perturbation patches located near the transmitter or receiver ($x = 10\lambda$) that lie on the GC path ($y = 0\lambda$) or 1 λ away from it ($y = 1\lambda$), and patches located at the GC path midpoint ($x = 400\lambda$) that also lie either on the GC path or 1 λ away from it. These outermost "arcs" of points in this figure correspond to a patch radius a of 10 λ. For the outermost sets of points in this figure, as one travels along an arc from the end nearest the $|\Delta\phi|$ axis towards the end nearest the $|\Delta A|$ axis, the regularly spaced grid location of the center of the patch is traversed from $x = 10\lambda$ to $x = 400\lambda$, while moving from arc to arc towards the origin corresponds to increasing distance away from the GC path (i.e., the y direction). The outermost set of arcs corresponds to the largest patch radius used. The relative probability of occurrence of different size patches or of different locations is not taken into account in this figure. The line represents a $|\Delta A|/|\Delta\phi|$ ratio of 0.14 dB/degree. (*b*) A plot similar to Figure 8*a* except that perturbed density profile III of Figure 3 was used in the calculations instead of profile I.

tered) magnitude $|e_n^s|$ and the 'echo' phase $\angle e_n^s$. Based on this assumption, they hypothesized that the expected value of the scattered magnitude and scattered phase was the same, i.e., $<e_n^s> \simeq <\angle e_n^s>$. This corresponds to a line drawn on a $|\Delta A|$-$|\Delta\phi|$ plot with a slope of 0.14 dB/degree. However, we find that based on our model, the results predict a different behavior for the scattered signal phase $\angle e_n^s$. It is interesting to note that when a line with slope 0.14

dB/degree is plotted in Figures 8*a* and 8*b*, it passes through the midst of many more of the points in plot *a* representing signal changes caused by a perturbation located at $L = 2$ than in plot *b* representing the same effect at $L = 3$. The 'average' slope of the envelope of points plotted in Figure 8*b* corresponding to perturbations at $L = 3$ is smaller than that of the envelope of points plotted in Figure 8*a* corresponding to perturbations at $L = 2$; and this 'average' slope is found to increase as the location of the perturbation causing the signal changes is moved to lower L-shells (using the density distribution model described by *Inan et al.* [1988*a*]). Thus, the 'average' slope of the envelope of $|\Delta A|$-$|\Delta\phi|$ points plotted for a perturbation located at or near Palmer, which is located at $L \simeq 2.3$, would lie somewhere between that of Figure 8*a*, corresponding to $L = 2$, and that of Figure 8*b*, corresponding to $L = 3$, being somewhat closer to that of Figure 8*a* than that of Figure 8*b*. It is interesting to observe that the theoretical 0.14 dB/degree slope calculated by *Dowden and Adams* [1988] also lies between the 'average' slope of the points of Figure 8*a* and that of Figure 8*b*, but is closer to that of Figure 8*a*. Thus, if the measured data points plotted in Figure 11*a* of *Inan and Carpenter* [1987] correspond to perturbations somewhere near Palmer (located, say, between $L = 2$ and $L = 2.3$), it may be fortuitous that a line with slope of 0.14 dB/degree passes through their midst.

Dowden and Adams [1988] suggest that the perturbation patch is an inverted pimple or 'stalactite' of small horizontal dimensions. The model described in this paper indicates that as the horizontal size (e.g., radius a) of the perturbation is increased, the magnitude of e_n^s also increases (Figure 6). For the realistic ionospheric parameters used in our calculations, we find that the change in effective reflection height (Δh) produced by perturbation profiles such as those shown in Figure 3 is small ($\Delta h \leq \sim 2$ km), and that patches with small ($a < 1\lambda$) horizontal extent simply do not diffract enough signal to affect the 'direct' signal e_n^o significantly. In most cases when $a < \lambda$, the value calculated for $|e_n^s/e_n^o|$ is much less than -30 dB, which was the typical value *Dowden and Adams* [1988] suggested according to their calculations for the strength of the scattered signal relative to the direct signal. *Dowden and Adams* [1989] suggest the existence of elongated perturbation stalactites or ridges produced by electron precipitation arcs aligned with an L-shell to explain Trimpi events measured at Dunedin, New Zealand. They again suggest that $\Delta h \simeq 15$ km which is much larger than what we find is produced by the density profiles used in our calculations. They explain that the location of such elongated stalactites is restricted to regions where some segment of an ellipse of constant echo signal delay (with the transmitter and receiver as foci) is within a few degrees of L alignment and suggest that the lack of this requirement may prevent the use of their model for explaining Trimpi events measured on other paths such as the NPM-Palmer path mentioned in this paper. A plan view of their ridge-like depression is approximately elliptical and is parallel to the NWC-Dunedin GC path. Equation (A16) of the Appendix to this paper indicates that the strength of the scattered field of an elliptical perturbation patch with Gaussian density distributions along each axis of the ellipse in the horizontal plane is linearly proportional to perturbation length parallel to the GC path. Thus, there is some similarity between the results of *Dowden and Adams* [1989] and our model. However, we note that our formulation assumes the density profile within and around the patch to be slowly varying (with vertical and horizontal distance) in order for mode coupling to be negligible and for the Born approximation to hold. Thus, a multiple-mode, non-Born-approximation model would be necessary to truly test the stalactite hypothesis.

For reasonable $S_n(r')$ shapes and ionospheric electron density profiles, we obtain values for ΔA and $\Delta\phi$ that are of the same order of magnitude as those measured on NPM–Palmer signals (i.e., $\Delta A \sim -0.3$ dB, $\Delta\phi \sim 3^\circ$). *Tolstoy et al.*'s [1986] multiple-mode 2-D theory predicts a range of values for ΔA and $\Delta\phi$ on the NPM–Palmer path of -0.08 to -0.34 dB and -0.46 to $+6.0$ degrees, respectively. Although some of these values are comparable to those of Figure 5, it is not possible to compare the results of our 3-D theory with the *Tolstoy et al.* [1986] 2-D theory since the *Tolstoy et al.* [1986] results include strong mode-coupling effects while our WKB theory neglects these effects. A new 3-D formulation which includes mode coupling would be needed to generalize the scattering problem.

5. SUMMARY AND CONCLUSIONS

We have presented initial results from a three-dimensional model of subionospheric VLF propagation in the presence of localized D region irregularities of the kind produced in lightning-induced electron precipitation events. This new formulation allows us to estimate the magnitude and phase of the field scattered from ionization perturbations which lie off the great circle path. Our results, using typical values for the ionospheric parameters, correspond well with actual values of amplitude and phase changes measured on a signal path having similar physical parameters as those assumed in the model, namely, single-mode propagation over a long sea-based path. It is found, for example, that modest ionospheric perturbations within $\sim 10\ \lambda$ of the GC path can produce amplitude and phase changes of the same sign and order of magnitude as the large majority of LEP events measured on the NPM signal at Palmer Station, Antarctica. The specific details of the altitude profile of the perturbation is found to have a significant effect both on the magnitude of the scattered signal and on the ratio of amplitude changes to phase changes caused by such a perturbation. In the context of lightning-induced electron precipitation, the perturbed profile produced by a precipitation burst at a lower L-shell has a higher density enhancement at lower altitudes, and produces a higher $|\Delta A/\Delta\phi|$ ratio, than does a profile produced by precipitation at a higher L-shell. We also find that the values of ΔA and $\Delta\phi$ can be used to give a rough estimate of the distance from the GC path to the perturbation.

Our model assumes that the ionization perturbation varies smoothly with radius and that a single mode is dominant. Our model can also be extended to the case of multiple modes in the WKB limit. However, more abrupt horizontal distribution profiles violate the slowly varying approximation, and thus, most likely produce additional modes through mode coupling. If this occurs close enough to the receiver that the additional modes are of comparable strength, effects more complicated than those predicted by a single-mode, or multiple-mode WKB, model would occur. Thus, a more encompassing multiple-mode model is needed to determine the phase or amplitude changes that an abrupt profile would produce, as well as to study cases where the GC path is relatively short, multiple modes of comparable amplitude

are propagating and impinging on the ionospheric perturbations, the path is over land of varying terrain as well as over sea, or any combination of these factors.

APPENDIX

Approximate Analytic Expression for the Scattered Field

According to *Wait* [1964a], the approximate normalized wave field for each mode scattered by an ionospheric perturbation of arbitrary horizontal extent can be expressed by the relation (the mode subscript n has been dropped in the following)

$$\frac{e^s}{e^0} = -(i)^{\frac{3}{2}} \frac{k_0 \alpha}{\sqrt{\pi}} [S(0,0) - S^0] I \tag{A1}$$

where

$$I = \iint_{\mathcal{P}} f(x,y) e^{-i\alpha^2 y^2} dx dy \tag{A2}$$

$$f(x,y) = \frac{S(x,y) - S^0}{S(0,0) - S^0} \tag{A3}$$

$$\alpha = \left[k_0 S^0 \frac{d}{2x_T x_R} \right]^{\frac{1}{2}} \tag{A4}$$

and where x and y are defined in Figure 1.

If we assume that the ionospheric density perturbation has a cylindrically symmetric Gaussian distribution in the horizontal plane, then according to equation (15) we can express (A3) in the form

$$f(x,y) = e^{-[(x-x_o)^2 + (y-y_o)^2]/a^2} \tag{A5}$$

where the position (x_o, y_o) represents the point of maximum perturbation. In order to integrate (A2) we will make use of the following identity from *Gradshteyn and Ryzhik* [1965]:

$$\sqrt{\frac{\pi}{q}} = \int_{-\infty}^{\infty} e^{-qp^2} dp \tag{A6}$$

where the real part of q is positive definite. Substituting (A5) into (A2) and using (A6) we obtain the expression

$$I = a\sqrt{\pi} \int_{-\infty}^{\infty} e^{-(y-y_o)^2/a^2} e^{-i\alpha^2 y^2} dy \tag{A7}$$

In order to integrate (A7), we first make the change of variable

$$z = y - \frac{y_o}{(1 + i\alpha^2 a^2)} \tag{A8}$$

With this variable change, (A7) becomes

$$I = a\sqrt{\pi} e^{-i\gamma} \int_{-\infty+i\epsilon}^{\infty+i\epsilon} e^{-(1+i\alpha^2 a^2) z^2/a^2} dz \tag{A9}$$

where

$$\epsilon = \frac{\alpha^2 a^2 y_o}{1 + \alpha^4 a^4} \tag{A10}$$

and

$$\gamma = \frac{\alpha^2 y_o^2}{1 + i\alpha^2 a^2} \tag{A11}$$

Since the integrand in (A9) is analytic everywhere in the finite complex z plane and vanishes at the endpoints, the integration contour can be moved to the real z axis without changing the value of the integral.

In this case, we can again make use of (A6) to evaluate (A9) and obtain

$$I = \frac{a\pi}{\sqrt{1 + i\alpha^2 a^2}} e^{i\gamma} \tag{A12}$$

Substituting (A12) into (A1), we arrive at the following analytical expression:

$$\frac{e^s}{e^0} = -(i)^{\frac{3}{2}} \sqrt{\pi} \frac{k_0 \alpha a^2 [S(0,0) - S^0]}{\sqrt{1 + i\alpha^2 a^2}} e^{-\eta \alpha^2 y_o^2} e^{-i\eta y_o^2/a^2} \tag{A13}$$

where $\eta = \alpha^2 a^2/(1 + \alpha^4 a^4)$.

According to (A13) the magnitude of the scattered field has the form:

$$\left| \frac{e^s}{e^0} \right| = \frac{k_0 \alpha a^2 |S(0,0) - S^0|}{(1 + \alpha^4 a^4)^{\frac{1}{4}}} e^{-\eta \alpha^2 y_o^2} \tag{A14}$$

Thus, the magnitude of the scattered field always decreases exponentially as a function of the distance of the perturbation from the GC path.

The development above can be generalized to the case in which the ionospheric perturbation has an elliptical cross-section for which

$$f(x,y) = e^{-[(x-x_o)^2/a_1^2 + (y-y_o)^2/a^2]} \tag{A15}$$

If (A15) is used in (A1), the development follows similar lines to yield

$$\frac{e^s}{e^0} = -(i)^{\frac{3}{2}} \sqrt{\pi} \frac{k_0 \alpha a_1 a [S(0,0) - S^0]}{\sqrt{1 + i\alpha^2 a^2}} e^{-\eta \alpha^2 y_o^2} e^{-i\eta y_o^2/a^2} \tag{A16}$$

where η is the same as given above. Since the quantity a_1 is a measure of the perturbation length parallel to the GC path, (A16) shows that the strength of the scattered field is linearly proportional to this length. To obtain the results of 2-D theory, let $a \to \infty$ to produce a perturbation strip of width a_1 along the GC path and which extends to infinity perpendicular to the GC path. For this case:

$$\frac{e^s}{e^0} = -i\sqrt{\pi} k_0 a_1 [S(0,0) - S^0] \tag{A17}$$

which is identical to *Wait*'s result [1964a] for the 2-D strip perturbation.

Acknowledgments. This research was sponsored by the Office of Naval Research under grant N00014-87-K-0299 to Stanford University. The MODEFNDR program used to determine the mode refractive indices was provided to us by J. A. Ferguson and F. P. Snyder of the Naval Ocean Systems Center (NOSC). We appreciate their support of this effort and our consultations with them on the use of the NOSC programs.

The Editor thanks A. J. Smith and another referee for their assistance in evaluating this paper.

REFERENCES

Budden, K. G., The numerical solution of differential equations governing reflexion of long radio waves from the ionosphere, *Proc. R. Soc. London, Ser. A, 227*, 516, 1955.

Budden, K. G., *Radio Waves in the Ionosphere*, Cambridge University Press, New York, 1961.

Budden, K. G., *The Propagation of Radio Waves*, Cambridge University Press, New York, 1985.

Carpenter, D. L., and J. W. LaBelle, A study of whistlers correlated with bursts of electron precipitation near $L = 2$, *J. Geophys. Res., 87*, 4427, 1982.

Dowden, R. L., and C. D. D. Adams, Phase and amplitude perturbations on subionospheric signals explained in terms of

echoes from lightning-induced electron precipitation ionization patches, *J. Geophys. Res., 93,* 11543, 1988.

Dowden, R. L., and C. D. D. Adams, Phase and amplitude perturbations on the NWC signal at Dunedin from lightning-induced electron precipitation, *J. Geophys. Res., 94,* 497, 1989.

Ferguson, J. A., and F. P. Snyder, The segmented waveguide program for long wavelength propagation calculations, *Tech. Doc. 1071,* Naval Ocean Systems Center, San Diego, Calif, 1987.

Gradshteyn, I. S., and I. M. Ryzhik, *Table of Integrals, Series, and Products,* Academic, San Diego, Calif., 1965.

Helliwell, R. A., J. P. Katsufrakis, and M. L. Trimpi, Whistler-induced amplitude perturbation in VLF propagation, *J. Geophys. Res., 78,* 4679, 1973.

Inan, U. S., and D. L. Carpenter, On the correlation of whistlers and associated subionospheric VLF/LF perturbations, *J. Geophys. Res., 91,* 3106, 1986.

Inan, U. S., and D. L. Carpenter, Lightning-induced electron precipitation events observed at $L \sim 2.4$ as phase and amplitude perturbations on subionospheric VLF signals, *J. Geophys. Res., 92,* 3293, 1987.

Inan, U. S., D. L. Carpenter, R. A. Helliwell, and J. P. Katsufrakis, Subionospheric VLF/LF phase perturbations produced by lightning-whistler induced particle precipitation, *J. Geophys. Res., 90,* 7457, 1985.

Inan, U. S., W. C. Burgess, T. G. Wolf, D. C. Shafer, and R. E. Orville, Lightning-associated precipitation of MeV electrons from the inner radiation belt, *Geophys. Res. Lett., 15,* 172, 1988*a*.

Inan, U. S., T. G. Wolf, and D. L. Carpenter, Geographic distribution of lightning-induced electron precipitation observed as VLF/LF perturbation events, *J. Geophys. Res., 93,* 9841, 1988*b*.

Lohrey, B., and A. B. Kaiser, Whistler-induced anomalies in VLF propagation, *J. Geophys. Res., 84,* 5121, 1979.

Morfitt, D. G., and C. H. Shellman, 'MODESRCH', an improved computer program for obtaining ELF/VLF/LF mode constants in an Earth-ionosphere waveguide, *Interim Rep. 77T,* Naval Electronics Laboratory Center, San Diego, Calif., 1976.

Rawer, K., D. Bilitza, and S. Ramakrishnan, Goals and status of the International Reference Ionosphere, *Rev. Geophys., 16,* 177, 1978.

Sheddy, C. H., A general analytic solution for reflection from a sharply bounded anisotropic ionosphere, *Radio Sci., 3,* 792, 1968.

Shellman, C. H., A new version of MODESRCH using interpolated values of the magnetoionic reflection coefficients, *Tech. Rep. 1143,* Naval Ocean Systems Center, San Diego, Calif., 1986.

Tolstoy, A., The influence of localized precipitation-induced *D* region ionization enhancements on subionospheric VLF propagation, Ph.D. thesis, Univ. of Maryland, College Park, 1983.

Tolstoy, A., T. J. Rosenberg, U. S. Inan, and D. L. Carpenter, Model predictions of subionospheric VLF signal perturbations resulting from localized, electron precipitation-induced ionization enhancement regions, *J. Geophys. Res., 91,* 13473, 1986.

Wait, J. R., Expected influence of a localized change of ionosphere height on VLF propagation, *J. Geophys. Res., 66,* 3119, 1961.

Wait, J. R., An analysis of VLF mode propagation for a variable ionosphere height, *J. Res. Natl. Bur. Stand., Sect. D, 66,* 453, 1962.

Wait, J. R., On phase changes in very-low-frequency propagation induced by an ionospheric depression of finite extent, *J. Geophys. Res., 69,* 441, 1964*a*.

Wait, J. R., Influence of a circular ionospheric depression on VLF propagation, *J. Res. Natl. Bur. Stand., Sect. D, 68,* 907, 1964*b*.

Wolf, T. G., Remote sensing of ionospheric effects associated with lightning using very low frequency radio signals, Ph.D. dissertation, Stanford Univ., Stanford, Calif., 1990.

U. S. Inan, T. F. Bell, and W. L. Poulsen, STAR Laboratory, Department of Electrical Engineering/SEL, Stanford University, Stanford, CA 94305.

(Received May 18, 1989;
revised September 5, 1989;
accepted September 7, 1989.)